Chapter 4

DFT

4.1 Introduction

As discussed in section 1.4, the majority of reports in the LENR field agree that high hydrogen loadings are either required or at least beneficial to observe excess heat. Several researchers reported superstoichiometric palladium hydrides (PdH_x with $x > 1$) [188, 189], however the experimental evidence of these is weak. While the mechanism of gas loading is rather simple and the major parameter to increase loading is increased pressure, the situation is more complicated with electrochemical loading. Several surface and bulk reactions must come together to result in hydrogen loading. To get a more quantitative understanding of these reactions and to inform our search for loading enhancers, we carried out DFT calculations.

4.2 Methods and Materials

In this section, we outline the methods used to probe electrochemical hydrogen loading in palladium and its compounds, in addition to synthesis and characterization protocols. Further details related to computational methods, particularly related to modeling of electrochemical processes in DFT, can be found in the Supporting Information (SI). The computational methods are briefly summarized in Scheme 4.1, where circles represent outcomes that are compared to experiment where possible.

4.2.1 Computational Methods

4.2.1.1 Density functional theory

Simulations utilized density functional theory (DFT) at the generalized gradient approximation (GGA) to probe energetics of relevant (electro)chemical reactions and bulk crystal optimizations. Surface reaction energetics (e.g., HER sub-reactions) were probed using the revised Perdew-Burke-Ernzerhof (RPBE) [190] exchange-correlation functional by Hammer and Nørskov. Bulk crystal energetics and dynamics were investigated using the PBEsol functional [191] which has been demonstrated here and in reported literature [192] to perform well in capturing bulk behavior. Given the significant difference in predicted lattice constant between RPBE and PBEsol, appropriate PdH_x bulk crystals were re-optimized with RPBE to minimize surface strain when probing surface processes. The Vienna Ab initio Simulation Package (VASP) [193–195]

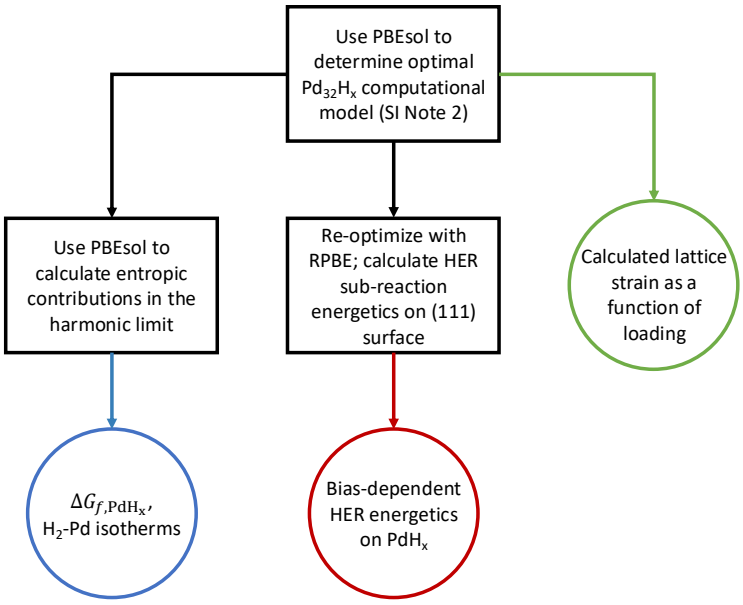

Fig. 4.1: Flowchart briefly illustrating computational methods described in more detail below and in greater detail in the SI. Here, circles represent outcomes that are compared to experiment where possible.

interfaced with the atomic simulation environment (ASE) [196] was used to perform all DFT calculations. For each atom in our simulations, core electrons were described using projector augmented wave (PAW) pseudopotentials, [197] while valence electrons were expanded as plane waves up to a kinetic energy cutoff of 500 eV. The Brillouin zone was sampled using a Monkhorst-Pack [198] k-point mesh, with the density depending on the system size. In general, the number of k-points multiplied by the magnitude of the unit cell vector in that dimension is approximately 30. For a 3×3×1 PdH_x(111) supercell, this corresponds to a 4×4×1 k-point mesh.

4.2.1.2 Surface reactions and free energy corrections

Gibbs free energies were calculated for gas phase molecules (e.g., H_2, H_2O) by making an ideal gas approximation. For reactions involving surface-bound species, e.g. *H, atoms were treated as having only vibrational degrees of freedom, and with those vibrational degrees of freedom treated harmonically. As such, the Gibbs free energy of reaction was calculated as,

$$\Delta G = \Delta E_{\text{rxn}} + \Delta ZPE - T\Delta S \quad . \tag{4.1}$$

Here ΔE_{rxn} refers to the reaction energy determined by DFT total energies, ΔZPE is the change in total zero point energy from initial to final state, and $T\Delta S$ is the entropic contribution to the Gibbs free energy. We neglect several possible entropic contributions, such as rotational and translational degrees of freedom, and anharmonic vibrational contributions. [199, 200] These approximations have been shown to be valid in the limit of small molecules on fairly strong binding surfaces. [201]

4.2.1.3 Gibbs free energies of formation of PdH_x

Similar to the calculation of surface reactions and their free energy corrections, we calculated the Gibbs free energy of formation of PdH_x ($\Delta G_{f,PdH_x}$) by determining the free energy of reaction of

$$\mathrm{Pd}(s) + \frac{x}{2}\mathrm{H_2}(g) \rightarrow \mathrm{PdH}_x(s) \quad . \tag{4.2}$$

Here, the entropic contributions of gas phase species (i. e., hydrogen gas) were determined in the ideal gas limit, taking into account translational, rotational, and vibrational degrees of freedom. Solid species (i. e., Pd and PdH_x) were determined in the harmonic limit using the CrystalThermo class implemented in the Atomic Simulation Environment. [196] Finite cell size effects were tested for smaller unit cells, with more details found in SI Note 5. For the Pd_{32} supercell, finite-cell size effects in the phonon spectra calculation were found to be negligible, and so a supercell size of (1,1,1) was used. In addition to entropic contributions arising from vibrational degrees of freedom in the crystal, we also included configurational entropy contributions associated with degenerate (or nearly degenerate) configurations of H via the equation,

$$S_{\mathrm{conf}} = k_{\mathrm{B}} \ln\left(\frac{N!}{n!(N-n)!}\right) \quad . \tag{4.3}$$

Here, k_{B} is the Boltzmann constant, N is the total number of available lattice positions (i. e., 32 for the Pd_{32} supercell), and n the number of H atoms in the supercell. We wish to highlight two caveats with this expression for the configurational entropy. First, this expression is a special case of Boltzmann's entropy formula, $S = k_{\mathrm{B}} \ln W$, for the case where the energy of each lattice position is identical. As we discuss below, generally this is not the case; H atoms seem to prefer maximal spatial homogeneity, disfavoring lattice positions close to another H atom except when no other sites are available. However, as we discuss further in the SI, the magnitude of the energetic penalty is relatively small, suggesting that this expression may be a reasonable approximation. Second, Equation 4.3 is valid only in the limiting case of large N. As a result, we compute S_{conf} using N=512, and $n = 16 * m$, where m is the number of hydrogen atoms in the Pd_{32} supercell. This correction is minor for the case of Pd_{32}, but the correction is significant for smaller supercells, e.g., Pd4 which has been previously reported. More details can be found in SI Note 6.

4.2.1.4 Modeling charge transfer processes in the grand canonical ensemble

For reactions involving charge transfer (e.g., the Volmer reaction), electrons were treated grand canonically as we have described in previous works. [202–205] Briefly, electrons are modeled as following proton transfer adiabatically in a coupled proton-electron transfer (CPET) reaction. Fractional electrons from an external reservoir compensate for transferred charge across the reaction coordinate, with countercharge being placed by solving the linearized Poisson-Boltzmann equation as implemented in VASPsol. [206–208] In addition to continuum solvation with a bulk dielectric constant set to 78.4, charged states (i. e., hydronium) were solvated with two explicit water molecules. We calculate the grand canonical free energy Ω as

$$\Omega = E - q\Phi \quad , \tag{4.4}$$

where E is the total energy from DFT, q the net system charge, and Φ the work function of the electrode. We refer the reader to previous works where we describe corrections required to account for the nonzero bulk electrolyte, [204] which can cause significant finite cell-height effects if uncorrected.

The overall thermodynamics of CPET reactions were modeled using the computational hydrogen electrode (CHE), [209] while activation barriers were estimated using our previously described [205, 210] one dimensional constrained bond length scan. In this approach, the O-H bond length for the transferring proton was systematically stretched, and the geometry optimized at constant potential subject to the fixed bond length constraint. The end result is an excellent estimate of the (grand canonical) energy surface, with the peak along the path taken to be the energy of the transition state. Given ongoing challenges with modeling hydroxide via semi-local DFT, [202,211] we considered hydronium (H_3O^+) as the proton donor for any CPET reaction. Activation barriers for non-CPET reactions (e.g., Tafel) were modeled using a machine-learning accelerated nudged elastic band routine which trains a Gaussian Process Regression model on-the-fly. [212] For additional details, we refer the interested reader to SI Note 1.

4.3 Results and Discussion

4.3.1 Experimental measurement of lattice strain in PdH_x

The XRD setup is illustrated in Fig. 4.2A). Details are provided in section 3.12. Panels B and C of Figure 4.2 show the transition from the α phase (which experiences minimal lattice strain) to the β phase, which starts highly loaded and increases in loading as well as in phase fraction as the loading progresses. Upon cessation of electrochemical bias (at 12 h), the lattice contracts and, as the bias is reversed, transitions back to the α phase, with some transient co-existence of α and β phases. The strain is calculated from the peak shift relative to the peak position of the initial pristine palladium sample. Various relationships between strain and loading have been reported (Figure 4.3A), some of them with greatly varying slopes. If the PBEsol strain-loading relationship is chosen, the relationship between resistance ratio (resistance normalized with initial resistance of pristine palladium) is in agreement with the relationship reported by Zhang [167] (Figure 4.3B).

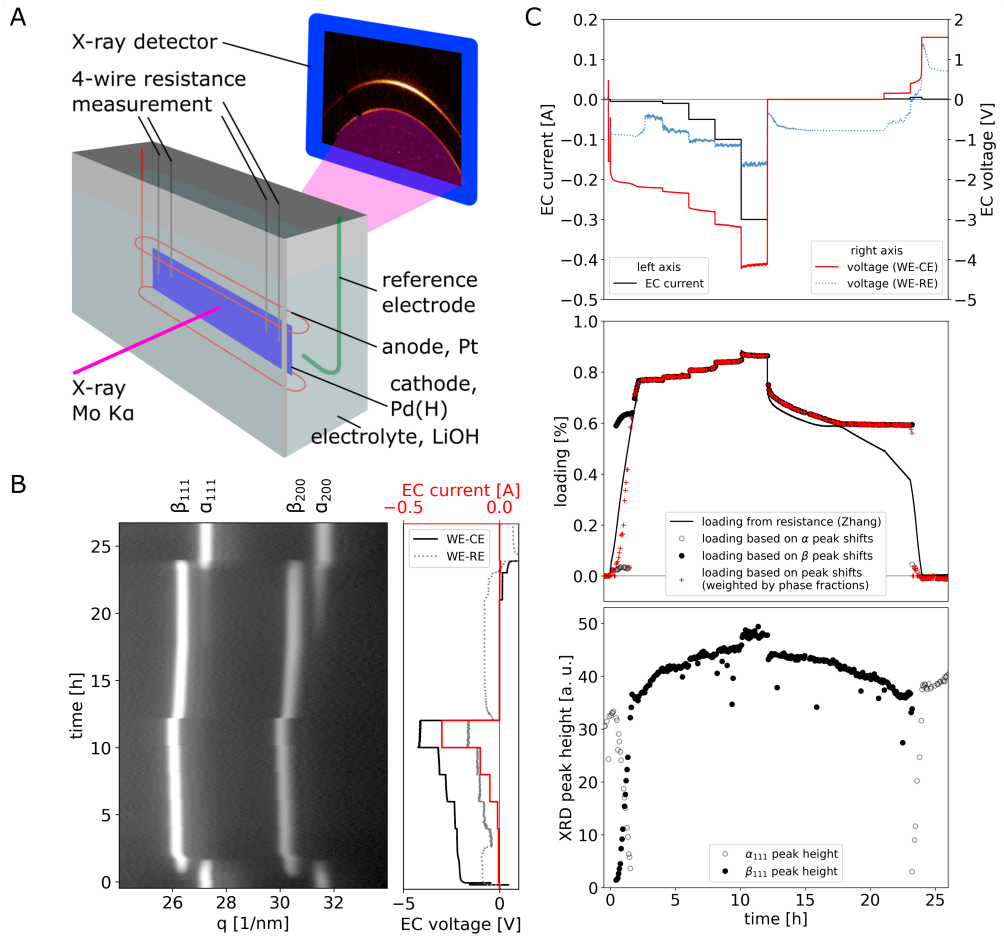

Fig. 4.2: XRD experiments to determine strain induced by hydrogen loading. (A) Schematic of the in-situ XRD electrochemical loading setup. (B) Waterfall plot obtained by stacking integrated XRD diffraction patterns of an in-situ loading experiment. Electrochemical current and voltage (between working electrode WE and counterelectrode CE as well as between working electrode WE and reference electrode RE) is plotted to the right. (C) EC current and voltage; loading obtained from the measured resistance ratio using the Zhang relationship (resistance ratio vs. loading), loading based on XRD strain using the PBEsol relationship (strain vs. loading); peak height of the α and β 111 peaks.

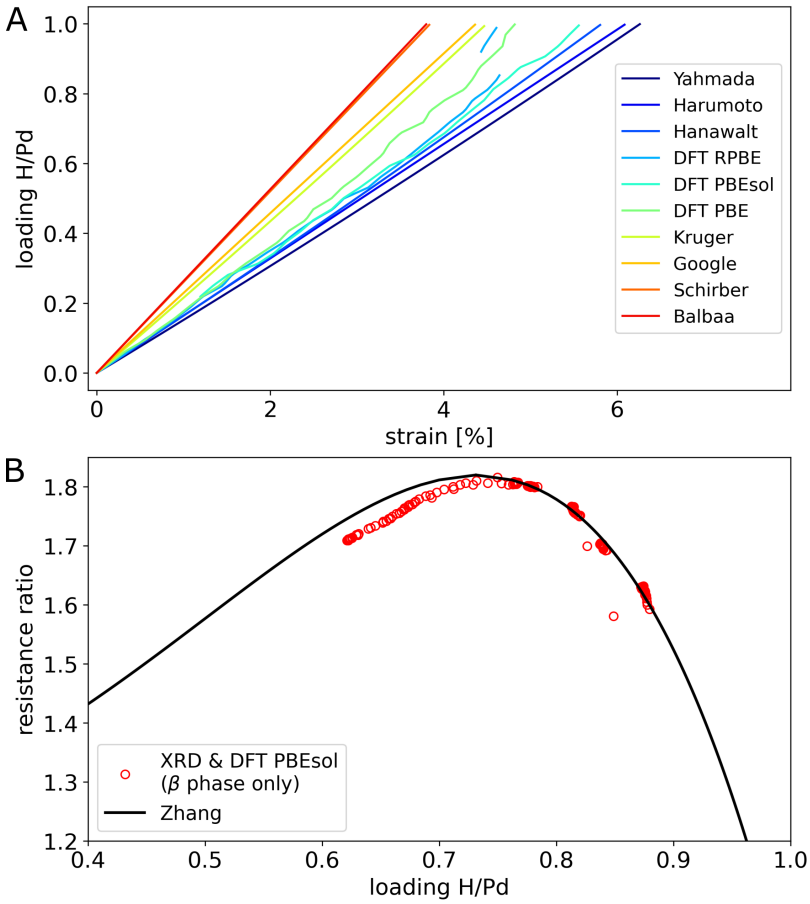

Fig. 4.3: (A) Strain-loading relationships reported in the literature by Yahmada [173, 174], Harumoto [175, 176], Hanawalt [173, 177], Kruger [178], Google [179], Schirber [173, 180], Balbaa [181]. (B) Resistance ratio vs. loading relationships. The black solid line is the curve reported by Zhang [167] and the red circles are from Figure 4.2C.

4.3.2 Development of a computational model of palladium hydride

To create a platform with which to probe hydrogen evolution reaction and intercalation energetics, we first generated a sequence of models for PdH_x, with x varying between zero and one in 33 increments. Briefly, we began with a 32 Pd atom supercell of $Pd_{32}H_{32}$, i. e. palladium hydride at stoichiometric loading, and systematically determine the most energetically favorable configuration with one hydrogen removed. By symmetry, all configurations of $Pd_{32}H_{31}$ are degenerate. To determine the optimal geometry for $Pd_{32}H_{30}$, we take the optimized geometry for $Pd_{32}H_{31}$ and generate all possible structures for $Pd_{32}H_{30}$; for this stoichiometry, there are 30 possible configurations. Each structure is then optimized using three separate semi-local DFT functionals: RPBE, [190] PBE, [213] and PBEsol. [191] Taking the lowest energy configuration, the process is repeated until $Pd_{32}H_0$ is recovered. Further details related to the protocol for generating these structures, and a more complete illustration of the Pd-Pd distance distributions can be found in SI Note 2. The result of these calculations was a library of structures for PdH_x as a function of loading x. An analysis of the library generated using PBEsol, with comparison to experimental measurements reported above, is given in Figure 4.4.

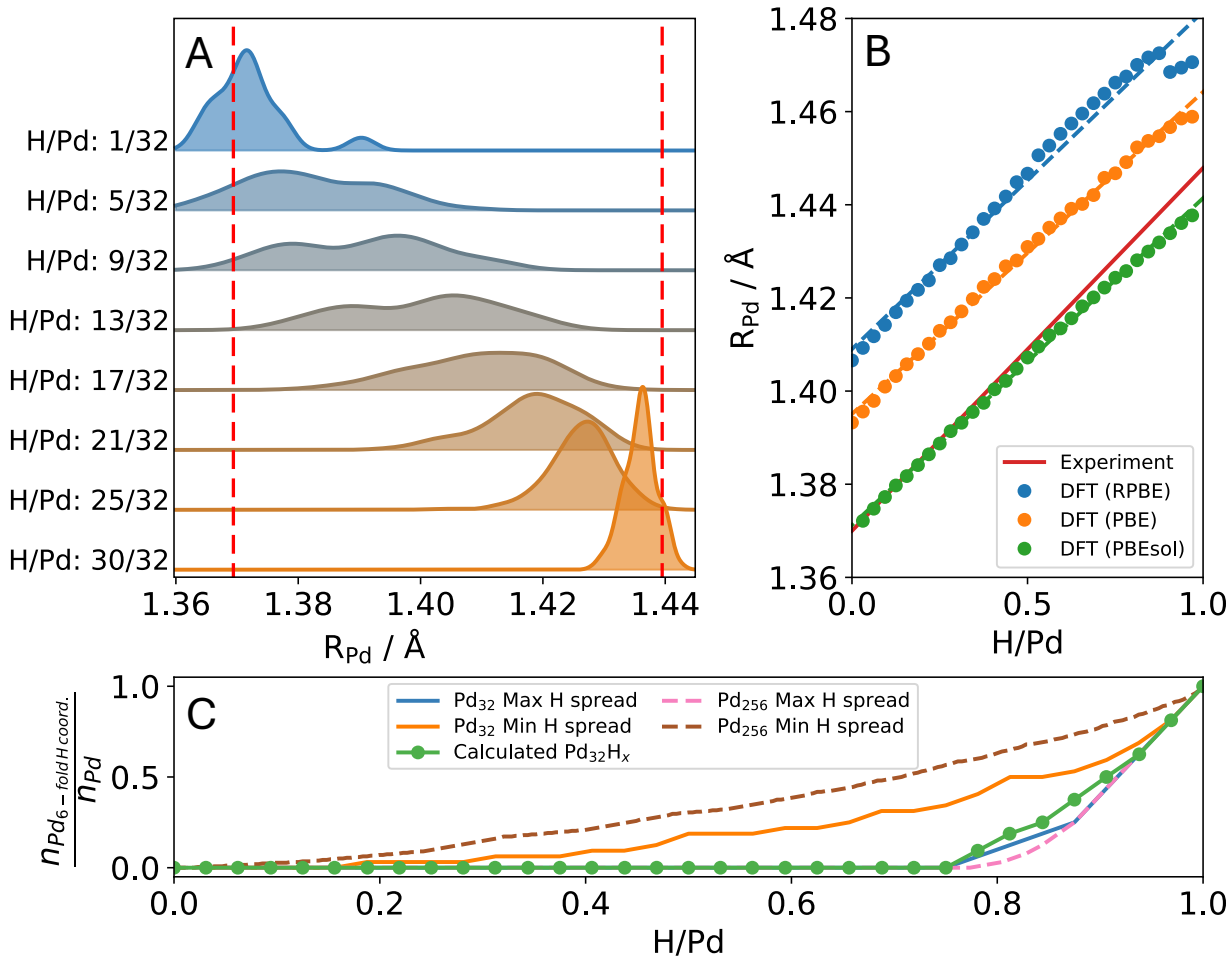

Fig. 4.4: (A) Distributions of Pd-Pd distances observed in the simulated $Pd_{32}H_x$ systems calculated using PBEsol, a semi-local density functional. Dashed vertical lines denote PdH_0 and PdH_1 lattice spacings. (B) Mean of the distributions for three different density functionals as a function of the hydride loading, with comparison to experimental measurements taken at near-stoichiometric loading. (C) Fraction of Pd atoms in Pd_{32} supercell that are 6-fold coordinated to hydrogen as a function of loading, with bounding cases for maximal and minimal hydrogen homogeneity.

In Figure 4.4A, we observe the characteristic two-phase coexistence of α- and β-PdH_x, as shown in the splitting of the Gaussian kernel density estimate [214] distributions at moderate hydride loading. Here, the two vertical dashed lines denote the average lattice spacing for PdH_0 (i. e., pure Pd) and PdH_1 calculated with PBEsol. We observe formation of two distinct peaks in the lattice spacing distribution as soon as a stoichiometry of 1/32, with the relative locations of each peak shifting as the loading is increased. At high loadings, approximately 25/32, the two peaks coalesce, consistent with β-PdH.

An analysis of the three semi-local density functionals considered in this work is shown in Figure 4.4B. Here, we report average lattice Pd-Pd (R_{Pd}) spacings as a function of hydride loading. As has been illustrated in previous literature, [215,216] the choice of functional has a significant impact on the predicted equilibrium lattice spacing. Although all functionals qualitatively capture the experimental trend of increasing lattice strain with higher loading (c.f. Figure 4.3), RPBE notably predicts an unphysical contraction of the Pd-Pd spacing at high loading, and is quantitatively the least accurate in predicting the correct lattice strain compared to modern experimental results. PBEsol in contrast is remarkably close to the experimental measurement, with moderate underprediction of the lattice spacing in the high-loading regime. Here we wish to highlight the substantial experimental uncertainty illustrated in Figure 4.3, and as such it is difficult to resolve whether the discrepancy between PBEsol and experiment in the high loading regime is due to the DFT, the experiment, or both. We further note that although our Pd-Pd spacing distributions reflect the two-phase coexistence of α- and β-PdH_x, this fine detail is lost in the averaging reported in Figure 4.4B. Since the peak locations shift to larger Pd-Pd spacings at higher loading, the net average Pd-Pd spacing (as would be determined from, e.g., XRD) is a smooth, monotonic increase.

Beginning with pure Pd, as the hydriding process occurs, the spatial distribution of hydrogen atoms is difficult to resolve experimentally. Neutron diffraction experiments suggest that H randomly occupies octahedral sites in the β-PdH_x phase, [217] but confirming with X-ray techniques may not be feasible. Hydrogen atoms may distribute homogeneously, preferring to spread apart, or may distribute heterogeneously, preferring to form hydrogen 'islands' within the bulk Pd. An analysis of this tendency for our PdH_x system is shown in Figure 4.4C. Here, we calculated the fraction of Pd atoms in our $Pd_{32}H_x$ supercell that have six hydrogen atoms as their nearest neighbor – corresponding to a fully occupied nearest neighbor octahedral sites. The blue line represents maximum hydrogen spatial homogeneity, a lower bound corresponding to hydrogen atoms preferring to coordinate to Pd atoms with minimal pre-existing H coordination. In orange is the opposite limit, representing minimal hydrogen spatial homogeneity, corresponding to the case where hydrogen atoms prefer to be coordinated to Pd atoms that are already highly coordinated. We find that, generally, hydrogen atoms prefer to be homogeneously distributed, with our calculated PdH_x system much more closely representing the lower limiting case. Dashed lines represent the same limiting cases as before, but for a Pd_{256} supercell rather than Pd_{32}. Here we can directly see the extent of a finite cell-size effect for our system. In the limit of maximum H spatial homogeneity, we observe a non-negligible finite cell-size effect, particularly in the region of H/Pd=0.8. A more detailed breakdown of H-coordination is shown in SI Note 3.

4.3.3 Isotherm analysis of the computational model of PdH_x

Given our computational model of PdH_x for $0 \leq x \leq 1$, we calculated the Gibbs free energies of formation as a function of both temperature and hydrogen pressure, illustrated in Figure 4.5(A) and (B) below.

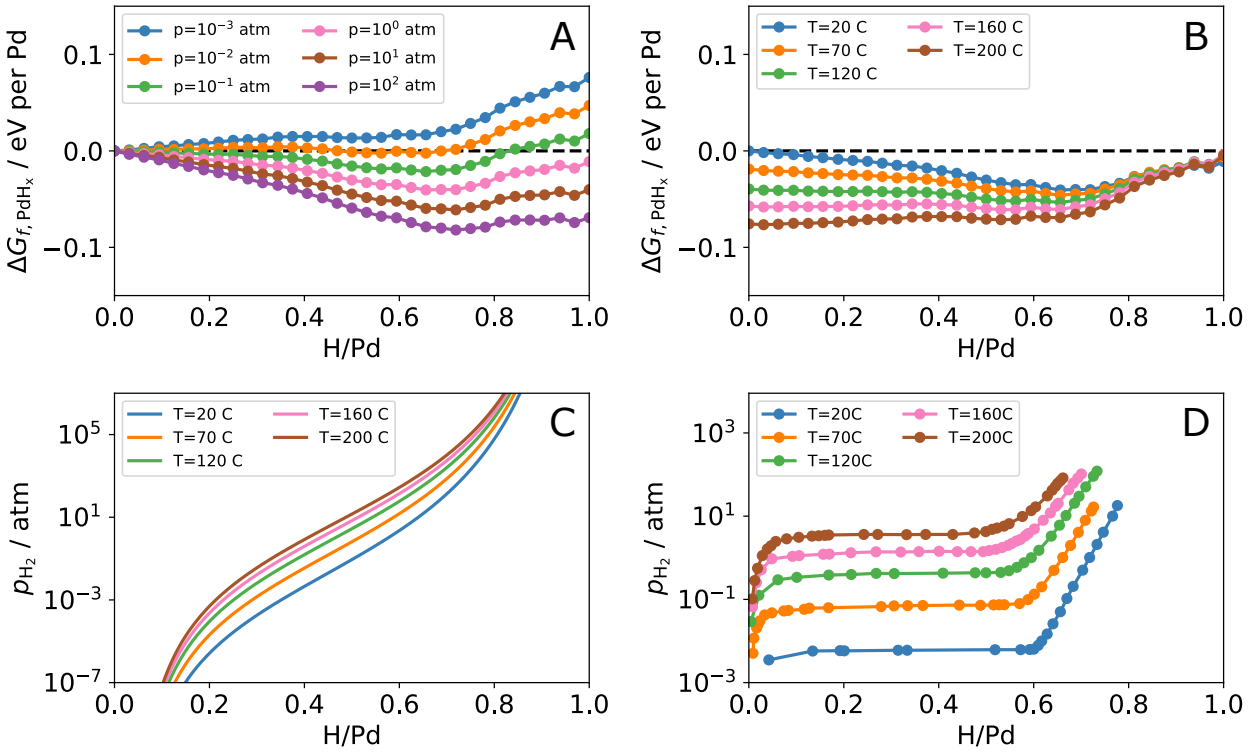

Fig. 4.5: Calculated Gibbs free energies of formation for PdH_x as a function of (A) H_2 pressure at T = 298 K, and (B) temperature at p_{H_2} = 1 bar. Additionally, (C) illustrates predicted temperature and pressure dependent isotherms, while (D) illustrates the experimentally measured isotherms. Panel (D) was adapted from Ref. [218].

Here $\Delta G_{f,\mathrm{PdH_x}}$ was determined with pure Pd metal and H_2 gas as the reference, with entropic corrections for the solid being determined in the harmonic limit (in addition to inclusion of configurational entropy), and with entropic corrections for the gas being determined in the ideal gas limit; more details can be found in the methods section. Reliable experimental references for $\Delta G_{f,\mathrm{PdH_x}}$ were not found for this system. However, reported enthalpies of formation ($\Delta H_{f,\mathrm{PdH_x}}$) show qualitatively similar behavior as a function of loading near standard temperature and pressure - convex with a minimum at H/Pd=0.5. [219] Given the configurational entropy contribution peaks at H/Pd=0.5, we hypothesize that the experimental $\Delta G_{f,\mathrm{PdH_x}}$ would show a minimum of H/Pd=0.7 as suggested by our calculations.

From the Gibbs free energies of formation and their temperature and hydrogen pressure dependence, we determined simulated isotherms for the PdH_x system, shown in Figure 3(C), with a digitized and re-plotted experimental reference [218] shown in Figure 3(D). For a given temperature and pressure, equilibrated loadings (i. e., H/Pd) were determined as a Boltzmann weighted average of the Gibbs free energies of formation, i. e.,

$$x = \mathrm{H/Pd} = \frac{\sum_i x_i \exp\left[-\frac{\Delta G_{f,\mathrm{PdH_x}}}{k_\mathrm{B}T}\right]}{\sum_i \exp\left[-\frac{\Delta G_{f,\mathrm{PdH_x}}}{k_\mathrm{B}T}\right]} \quad . \tag{4.5}$$

Here, x represents the equilibrated H/Pd ratio, and x_i are the incremental H/Pd ratios at which we determined $\Delta G_{f,\mathrm{PdH_x}}$, i. e., ranging from 0 to 1 in 33 total increments for the Pd32 supercell. Although our simulated isotherm agrees reasonably well, qualitatively, with the experimental reference (higher equilibrium loading at lower temperature and higher pressure, three apparent regimes at low, medium, and high loading), our isotherm does not capture the two-phase coexistence of the α- and β-PdH_x denoted by the flat regions in the isotherm at moderate loading. We hypothesize that this may be due to finite cell-size effects, as suggested by nanoscopic PdH_x synthesis and characterization experiments from the groups of Schmid-Ott and Zoric, [220, 221] who similarly report no two-phase coexistence regime between the α- and β-PdH systems. The former study, which reported synthesis of nanoscopic rings of varying thickness and associated isotherms, suggests that length scales on the order of 100 nm would be necessary to capture the two-phase coexistence regime, which is computationally intractable at the GGA-DFT level of theory.

4.3.4 Unraveling the interplay between hydrogen evolution and electrochemical loading

Unlike gas-phase loading of Pd, electrochemical loading is driven by the applied bias, producing adsorbed hydrogen atoms on the surface which then intercalate given sufficient driving force and facile kinetics. Considering the equilibrium between the bulk hydride phase and the electrolyte, at first glance this seems to be a very attractive route to achieving higher bulk loadings. A simple analysis of the thermodynamics in the bulk-to-bulk equilibrium formalism would suggest that linearly changing the applied bias is equivalent to logarithmically changing the hydrogen pressure. In other words, considering just the bulk phases, utilizing an easily achievable applied bias would lead to loading driving forces that are equivalent to gas-loading pressures that are not realistic with current capabilities. [222] However, in reality, equilibrium between these two bulk phases is never achieved, as a third phase must be considered – the surface – which ultimately prevents equilibration, since surface-bound hydrogen reacts to form molecular hydrogen via the hydrogen evolution reaction (HER) faster than intercalation.

Towards unraveling this complex co-dependency, we calculated the dependence of the three HER sub-reactions on the surface hydrogen coverage θ_H, applied bias U, and hydrogen loading x. Specifically, the three HER sub-reactions considered are,

$$\text{Volmer}: \quad (\mathrm{H}^+ + e^-) + * \rightarrow *\mathrm{H} \tag{4.6}$$

$$\text{Tafel}: \quad 2 * \mathrm{H} \rightarrow 2 * + \mathrm{H}_2(g) \tag{4.7}$$

$$\text{Heyrovsky}: \quad (\mathrm{H}^+ + e^-) + *\mathrm{H} \rightarrow * + \mathrm{H}_2(g) \tag{4.8}$$

Energetics for all three sub-reactions were calculated, but primary focus was on the Volmer and Tafel reactions, as experimental Tafel slope analysis suggests that PdH_x operates in a Volmer-Tafel limiting regime. [223] Briefly, multi-feature linear regression models were fit for the Volmer and Tafel reaction to capture the (inter-)dependence of the sub-reaction energetics on θ_H, U, and x. Contour plots illustrating the fit models are shown in Figure 4.6. Further details related to the calculated energetics, computational geometries, thermodynamic references utilized, and parameters for the multi-feature linear regression model are given in SI Note 4. Additionally, all DFT input and output files used in producing these figures can be found

in a separate electronic supporting information zip archive. Note that the Tafel energetics reported here correspond approximately to enthalpies, rather than Gibbs free energies. We expect the entropic contribution would be an approximately constant shift over the investigated energetic landscape, and the choice of pressure for the gas-phase H_2 product would introduce substantial uncertainty into the magnitude of this shift, and as such we choose to report the enthalpy.

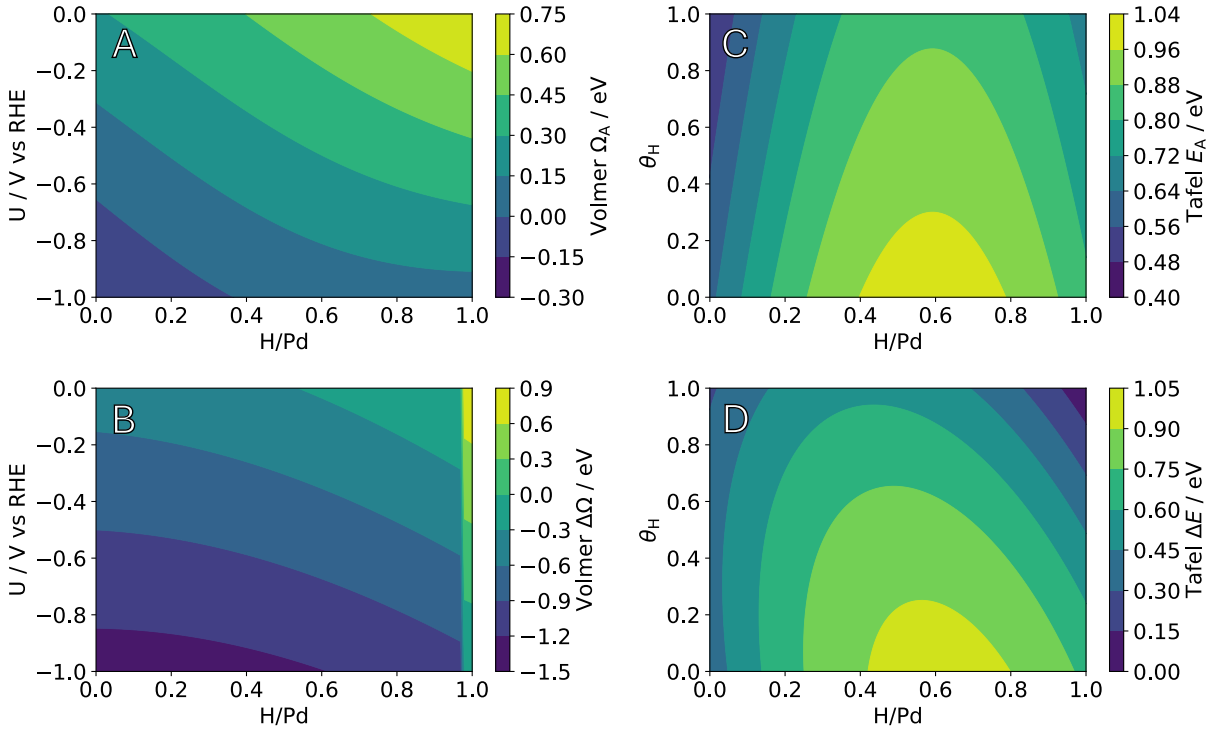

Fig. 4.6: Computed hydrogen evolution reaction (HER) sub-reaction energetics. (A) and (B) illustrate proton reduction (i. e., the Volmer reaction) activation barriers and reaction energies, respectively, as a function of loading and applied bias. Energetics here were calculated treating electrons grand canonically, as described in the methods section. Panels (C) and (D) illustrate molecular hydrogen production activation barriers and reaction energies, respectively, driven by the Tafel reaction.

As the H loading increases at a fixed applied bias, we find a significant increase in the bias-dependent Volmer activation barriers reported in Figure 4.6A. Higher barriers suggest reduced overall activity towards the HER at high loading, and is consistent with weaker H-binding found at high loadings. We note that the reported negative activation barriers are caused by utilizing bulk protons as the energetic reference (i. e., via the CHE) for the transition state energy; a small, exergonic energy change is associated with bringing a proton from the bulk electrolyte to the reaction plane under reducing conditions. Similarly, we find generally increasing (i. e., less favorable) Volmer reaction energetics as the H loading increases at a fixed bias, as shown in Figure 4.6C. The energetics become particularly less favorable as the loading approaches 100 % (H/Pd =

1.0). For loadings > 97 %, the favorable 3-fold binding sites that H prefers are no longer available, forcing H into a less favorable binding configuration (see SI Note 7), explaining the step increase in Volmer $\Delta\Omega$ visible in Figure 4.6C.

We wish to highlight the very strong dependence of the Tafel reaction on surface H coverage θ_H. Indeed, for coverages > 1 (i. e., all 3-fold hollow sites occupied , consistent with the step increase in Volmer reaction energetics, see SI Note 7), the Tafel reaction is barrierless and has a strong exergonic driving force. From our calculations it is difficult to determine a steady-state θ_H without implementation of a microkinetic model. Given the clear dependence of the critical reaction energetics on local structure, a mean-field approach is likely insufficient. Determination of the steady-state θ_H would therefore likely require, e.g., a kinetic Monte Carlo approach, which is beyond the scope of this study but would be an interesting area of future work. However, given facile (de)intercalation as evidenced by observation of hydride formation at potentials > 0 V_{SHE} and spontaneous deintercalation of bulk H at low θ_H or high H/Pd, we anticipate that at steady-state, θ_H should be at least of a similar magnitude to the loading H/Pd, i. e., $0 \ll \theta_H < 1$.

4.3.5 The cause of the upper bound on electrochemical loading of palladium hydride

Experimentally (see Figure 4.2C), the loading is observed to have an upper bound of approximately 0.7-0.85, far lower than the equilibrated loadings predicted theoretically. [222, 224] Based on the results of our computational model of PdH_x and calculated HER sub-reaction energetics we hypothesize the cause for this sub-unity upper bound on electrochemical hydrogen loading to be a confluence of several factors. First, and perhaps most importantly, at high surface H coverages $\theta_H \to 1$, the Tafel activation barrier peaks at around 80 % loading, before quickly decreasing. For $\theta_H > 1$, corresponding to > 1 H per surface Pd (with Hs occupying the 3-fold hollow site), the Tafel reaction is calculated to be barrierless – meaning that the Tafel reaction rate is determined entirely by the attempt frequency in the pre-factor of an Eyring-like expression. In other words, the surface coverage will likely never exceed 1 H per surface Pd on timescales relevant for H intercalation, imposing an upper bound on the possible electrochemical driving force for H loading, far below the driving force one obtains when neglecting the surface.

In addition to the dynamic changes in HER catalysis with increasing loading, we found the differential Gibbs free energy of formation of PdH_x to become positive (i. e., endergonic) for loadings above 70 %, depending on the pressure (Figure 4.5). The change in sign for the differential Gibbs free energy of formation is likely driven by the requirement of filling the 6th octahedral site of Pd above about 70 % loading, as discussed in SI Note 3. Filling this last octahedral site is energetically unfavorable, requiring an increased driving force to exceed 70-80 % loading.

Given the above factors imposing a fundamental limit on electrochemical H loading, strategies to go beyond this limit must focus on either inhibiting the Tafel reaction (i.e., Tafel poisons), ideally without simultaneously hindering H intercalation and without accelerating the Heyrovsky reaction or impeding the Volmer reaction. Alternatively, identification of materials with more favorable hydride formation energetics may be able to undergo electrochemical loading with lower θ_H, which would inhibit both the Tafel and Heyrovsky reactions.

4.4 Conclusions

To summarize, in this work we developed a novel computational model of palladium hydride at incremental hydrogen loadings, with the resulting lattice spacings validated by operando experimental XRD measurements. From this computational model, we calculated Gibbs free energies of formation which were used to simulate gas-loading isotherms of PdH_x. From these simulated isotherms, we found that the well-known two-phase coexistence of α- and β-PdH_x is a macroscopic phenomenon, in support of experimental measurements of gas-loading isotherms on nanoscopic samples of Pd. By cutting a (111) surface of PdH_x at incremental loadings and calculating HER sub-reaction energetics at different potentials, loadings, and surface coverages, we determined that dynamic changes in the energetics of these crucial sub-reactions impose an upper bound on the feasible electrochemical loading of Pd. In contrast to a simple thermodynamic analysis of the equilibrium between bulk PdH_x and protons/electrons, which would suggest that superhydride formation is feasible at reasonable conditions, our analysis incorporating HER catalysis supports experimental measurements of a maximum 70-80 % hydride loading by electrochemical means in Pd. Our results suggest that incorporation of the surface phase is critical when examining new materials for electrochemical hydrogen storage. By suppressing the Tafel reaction, electrochemical loading may be enhanced, but equilibration between the bulk PdH_x and electrolyte phases is unlikely. An interesting area of future work will be to incorporate the energetics and active loading dynamics into a kinetic Monte Carlo calculation, which may reveal finer-grain details relating the interplay between HER energetics and electrochemical H storage in different metal hydrides.